Article

A Comparative Study of Oxygen and Hydrogen Adsorption on Strained and Alloy-Supported Pt(111) Monolayers

Ian Shuttleworth

School of Science and Technology, Nottingham Trent University, Nottingham NG11 8NS, UK;
ian.shuttleworth@ntu.ac.uk

Abstract: A comparative study of the unreacted and reacted uniaxially strained Pt(111) and the layered (111)-Pt/Ni/Pt$_3$Ni and (111)-Pt/Ni/PtNi$_3$ surfaces has been performed using density functional theory (DFT). An in-depth study of the unreacted surfaces has been performed to evaluate the importance of geometric, magnetic and ligand effects in determining the reactivity of these different Pt surfaces. An analysis of the binding energies of oxygen and hydrogen over the high-symmetry binding positions of all surfaces has been performed. The study has shown that O and H tend to bind more strongly to the (111)-Pt/Ni/Pt$_3$Ni surface and less strongly to the (111)-Pt/Ni/PtNi$_3$ surface compared to binding on the equivalently strained Pt(111) surfaces. Changes in the surface magnetisation of the surfaces overlaying the ferromagnetic alloys during adsorption are discussed, as well as the behaviour of the d-band centre across all surfaces, to evaluate the potential mechanisms for these differences in binding. An accompanying comparison of the accessible density functionals has been included to estimate the error in the computational binding energies.

Keywords: Pt-Ni catalyst; strain engineering; bimetallic surfaces; density functional theory; DFT

1. Introduction

Understanding the mechanisms of the use of the oxygen reduction reaction (ORR) and the hydrogen evolution reaction (HER) is key to the development of modern energy storage and transport materials. The technology inherent in these materials contributes significantly to sustainable chemical production, whose energy footprint is an imperative concern when designing catalysts and networks of catalysts.

There are several different ways that catalytic surfaces can be trained towards a particular reaction sequence or energy budget. Lattice strain control [1] has been conceptually available for several decades [2] and generally involves applying biaxial or, less commonly, uniaxial strain within the surface plane of the catalyst. There are a number of possible consequences of this action, and their relative importance depends sensitively on a number of factors, including the stoichiometry and structure of the catalyst under investigation, the working conditions of the catalysts, the way that the strain is applied and the type of investigation being performed. In the latter point, the main distinction made in the current work is between investigations which are performed experimentally and those that are performed theoretically, or computationally. In these latter investigations, systems are reduced in their complexity, such as the trial systems commonly presented in density functional theory (DFT) investigations. Other computational methods can model larger systems and investigate larger scale phenomena, e.g., reaction processes around extended surface clusters, but the computational tools used, such as empirical force fields, require considerable refinement and training to produce simulations which are physically meaningful.

The current manuscript is a purely computational work. However, it is worthwhile to review some of the more important experimental phenomena observed to reinforce the importance of some of the investigations that will be performed in the current work and how applying strain can enable some of these phenomena. Fundamentally, there are three classes of phenomena: ensemble, ligand and geometric. Ensemble effects occur when

dissimilar species that form small groups (ensembles) acting individually demonstrate distinct mechanistic characteristics. These groups can form on a surface by, for example, relaxing the surface tension and applying heat: this reduces the energy barriers to diffusion and provides individual atoms with sufficient energy to move between binding positions. Ligand effects are associated with charge transfer between atoms, and geometric effects are associated with the relative position of atoms. These latter effects are the primary control in the current work, as the strain applied in the current simulations will move the surface atoms either closer together or farther apart. They can also manifest in a way similar to the ensemble effects earlier: if, for example, a surface phase transition is encountered under strain, then the symmetry and surface structure can change significantly.

Though these effects are often presented in the literature separately, they often intermix. Ligand and ensemble effects can often accompany changes in surface strain. For a clean surface of a pure material, this phenomenon is well understood: the number of bonds that atoms in the surface layer form are different from the those that atoms in deeper layers will form, and consequently an internal strain arises. This phenomenon can be extended to the cases of thin film growth where an overlayer is deposited on a substrate of a different material. In this case, in addition to the differences in valence between the atoms in the overlayer compared to their valence in bulk form, a lattice mismatch may also exist between the deposited layer and the substrate, internally straining the deposited layer. These phenomena have been described in terms of single crystal systems which are of significant interest to computational researchers—particularly those specializing in density functional theory and ab initio methods—as they are computationally accessible. However, several related phenomena exist which are of more interest to experimental teams or practitioners of force-field techniques. These phenomena exist across nanoparticles, which because of their large surface area, are particularly practical catalysts. Reducing the size of the nanoparticles will generally reduce the size of the lattice constants of these particles [3] as a way of relieving changes in the surface energy. This phenomenon becomes more complex in the case of bimetallic and alloy systems where, as well as changes in the surface strain and energy, thermal processing of the nanoparticles—a common feature in modern catalysts, which are often run at elevated temperatures—will cause the formation of pure metal overlayers. This is the case in the current investigations into Pt_xNi_{1-x} and is central to the investigations in the current work.

The application of mechanical strain to a surface can also effect changes to the reactivity of the surface and its effectiveness as a catalyst. For example, applying a uniaxial compression to Pt(100) [4] causes a reduction in the energy difference between the initial and transition state energies, breaking the scaling catalysis laws [5] and improving the effectiveness of the surface as a catalyst. In addition [4], several auxiliary promotion methods, including the application of magnetic and electric fields, have been observed experimentally for similar systems.

Recent experimental studies [6] have used aberration-corrected high-resolution transmission electron microscopy on Pt−Fe alloy core-shell nanoparticles with Pt-rich surfaces to directly evidence the presence of lattice strain and its effect on oxygen reduction reactivity. More generally, the experimental technique of seed-mediated coreduction (SMCR) has recently been developed [7] and allows PtM (where M = Ni, Co, Cu or Fe) shells to be deposited on intermetallic seeds. The performance of these nanocatalysts has been significantly better than the equivalent Pt reference, with PtCu and PtNi shells notably demonstrating a 230% and 270% activity increase in activity towards the oxygen reduction reaction (ORR). Pt-skinned $CoPt_x$ [8] has shown similar effectiveness towards the hydrogen evolution reaction (HER). Equally, the application of external strain to Pt(111) has been shown to improve the rate of formate yield during formic acid oxidation [9]. Improvements in activity are not simply confined to materials with Pt incorporated into a surface layer. The manipulation of Ni_3Fe thin films via externally applied strains [10] has been shown to control the activity of the electrocatalytic oxygen evolution reaction (OER). This study is significant in the current context, as both Ni and Fe are ferromagnetic compared to the nonferromagnetic Pt; the importance of this

ferromagnetism and its relative importance to the externally applied strain have not been fully investigated in the original work [10] or in subsequent publications but may prove significant.

Based on the current published database of catalyst performance, some systematic design protocols have been proposed. Examples of the design protocols have been based on the chemical composition, atomic coordination, and strains of the top surface layers of nanocatalysts [11]. Other examples use strain engineering and localized lattice strain [12], which focuses development on the d-band model of surface reactivity and the known high reactivity of defects compared to defect-free surfaces and facets. The importance of defects and subsurface vacancies has been shown in fundamental studies of Pt-based catalysts [13]. Further protocols have focused on ensemble effects in Pt overlayer [14] using a kinetic-mapping technique.

Whilst these broader characterizations have demonstrated some success, there is still the need to develop a fundamental understanding of Pt-based catalysts—for example, in the empirical modelling of the pure metal under strain [15]—as a characterization and potential systematic design tool. This approach has been applied, in part, in recent studies which evaluated both the strain and the ligand effects [16] by systematically geometrically constraining Pt-bearing nanoparticles but allowing adsorbates to fully relax on them. These studies identified Pt–Au–M nanoparticles (M = Cr, Mn, Co, Cu, Zn) as promising electrocatalysts for the ORR, due to their inherently weak Pt–OH binding with respect to a pure Pt nanoparticle. This fundamental approach highlights the importance of single crystal methods, e.g., [17], even amongst the literature which is increasingly dominated by nanoparticle and multiple-facet studies, and as an essential part of the important bridging studies [18,19] between the more idealized single crystal methodology and the less computationally accessible nanoparticle simulations. One recent example of single crystal studies has been a broad survey [20] of low index transition metal surfaces and their potential reactivity towards the HER. This survey concluded that under applied strain, the hydrogen atoms across a range of surfaces could migrate between preferred binding sites with a concurrent change in local valence, binding energy, and potentially significant changes to their reactivity.

The current work will focus on density functional theory investigations of single crystal systems. This approach has very recently proven successful in determining the stability of Pt skins overlying a range of intermetallic layers [21] and in the activity of Pt/PtV(111) towards the ORR [22]. The current investigations will focus on the multi-layered (111)-Pt/Ni/Pt$_3$Ni and (111)-Pt/Ni/PtN$_3$i using a full spin-polarized approach. Recent studies [23] of the magnetic character of the ordered bulk L$_{10}$ and L$_{12}$ phases of Pt$_3$Ni, PtNi and PtNi$_3$ using both scalar and vector relativistic density functional theory (DFT) have shown that the effect of applying compressive or tensile strain to each alloy is to decrease or increase the magnetism of the alloy, respectively. The Pt$_x$Ni$_{1-x}$ bulk alloys considered in that work [23] are part of a series of experimentally accessible alloys, which include Pt$_x$M$_{1-x}$ (M = Fe,Co), and therefore, each contain a permanently magnetised (Ni, Fe or Co) component. Comparative studies of these materials are therefore beneficial as they can highlight trends within this class of bimetallics. The response of the magnetic moment of the L$_{10}$ and L$_{12}$ ordered phases of Pt$_3$M, PtM and PtM$_3$ (M = Fe,Co) to compressive and tensile strain [24] has shown that the magnetic moment of the Pt$_3$M and PtM phases varies linearly with applied strain. The response of the PtM$_3$ alloys shows significant transition in the rate of change of magnetic moment at approximately zero strain. The magnetic moment changes of Pt$_x$Fe$_{1-x}$ and Pt$_x$Co$_{1-x}$ during strain arise from intraorbital charge transfer between d orbitals. These background studies demonstrate some of the characteristics of the ordering of the substrate layers considered in the current work.

The computational investigations in the current work have been prompted by the experimental observation [25] that the Pt$_3$Ni(111) activity towards the ORR is 10-fold the activity seen on Pt(111), and similar observations have been made on Pt$_3$M surfaces [26]. Due to the technological importance of both the HER and ORR systematic investigations, a systematic series of DFT investigations have been completed for the strained H/Pt(111) [27], O/Pt(111) and OH/Pt(111) [28] systems. These investigations have shown that for the H patterned surfaces,

and for smaller unit cells of the oxygenated surfaces, applying biaxial strain in the surface (111) plane changes the lowest energy binding position of the adsorbate. This result is of fundamental importance, particularly with adsorbates that have directional bonds with the substrate, such as oxygen, because changing the valence of these adsorbates with the surface will significantly change the available valence charge of that adsorbate to other reacting molecules.

Single crystal experimental studies of the $Pt_3Ni(100)$, (110) and (111) [29] have demonstrated that some refinement of the single overlayer model routinely used in computational investigations in this field is necessary. After thermal processing of nanoparticle Pt_3Ni, a conventional core-shell structure develops composed of pure metal overlayers and an alloy. However, in the case of the Pt_xNi_{1-x}, the Pt surface layer has been shown to lie on a purely Ni second (selvedge) layer. The current work will therefore investigate the effect of this magnetic selvedge layer. The current work will also investigate the effects of unit cell size during the oxygenation of Pt(111) under strain and will further provide a benchmark equation of state and surface energy data for the clean Pt(111) under strain. These investigations will quantitatively evaluate the density functional used and seek to establish a broad computational error bar in the binding energies and bond lengths, determined using both local density approximation (LDA) and the generalised gradient approximation (GGA).

2. Computational Methods

The investigations performed in this work used the Quantum Espresso density functional theory (DFT) package [30]. Spin-polarized simulations were performed using both the local density approximation (LDA) and the generalized gradient approximation (GGA). Hybrid functionals, which would nominally have required an order of magnitude more computational time, were not considered in the current work.

The reason that the two sets of calculations were performed was to estimate the computational error in the current set of investigations, which will assist experimental teams who may wish to compare their experiment results with the results presented in the current work. The reason that these two approximations were used was because the current work focusses on the bond lengths and the cohesive, surface and adsorption energies. The LDA is conventionally found to overestimate cohesive energies and underestimate bond lengths. The GGA tends to overcompensate for the LDA overbinding and consequently overestimates the bond lengths. Comparative studies of the two functionals can then at least approximately provide an upper and lower estimate of the expected values of these quantities. Furthermore, the two functionals are computationally accessible for the size of systems that are being investigated in the current work.

The Perdew–Zunger (PZ) LDA and the Perdew–Burke–Ernzerhof (PBE) GGA exchange-correlation functionals were used to generate the norm-conserving pseudo-potentials [31] used in the current simulations. A wave-function kinetic energy cut-off of 75 Ry and a charge density/potential cut-off of 300 Ry were used throughout these investigations, and a Brillouin zone sampling of ($10 \times 10 \times 10$) and ($6 \times 6 \times 1$) was used for the bulk and surface investigations, respectively. A first-order Methfessel–Paxton smearing of 0.02 Ry is used throughout this work [32].

The cohesive energy E_{coh} of the bulk Pt crystal is defined in Equation (1):

$$E_{coh} = E_{bulk} - E_{iso} \tag{1}$$

where E_{bulk} is the energy of the primitive bulk crystal, which contains 1 Pt atom/unit cell. E_{iso} is the energy of a single Pt atom in the gas phase, which was calculated by setting the atom in an orthogonal box with dimensions $10 \times 10 \times 10$ Å^3. ($1 \times 1 \times 1$) unit cells were used to perform the bulk Pt and bulk alloy investigations.

The surface energy E_{surf} of the clean Pt(111) slab was calculated using Equation (2):

$$E_{surf} = \frac{1}{A}(E_{slab} - nE_{bulk}) \tag{2}$$

where A is the total surface area of a slab containing n atoms with a total energy E_{slab}. (1×1) surface unit cells were used to perform the unreacted (clean) Pt(111) investigations.

The energies E of any density of states which have been considered in this work are normalized to the Fermi level E_F, i.e., $E_F = 0$ eV. The centre E_c and width w of each of the density of states $P(E)$ are defined in terms of their first and second moment, respectively [33].

$$E_c = \frac{\int_{-\infty}^{\infty} EP(E)dE}{\int_{-\infty}^{\infty} P(E)dE} \tag{3}$$

$$w = \frac{\int_{-\infty}^{\infty} (E - E_c)P(E)dE}{\int_{-\infty}^{\infty} P(E)dE} \tag{4}$$

Strain σ was defined in Equation (5) in terms of general lattice constants L and L_0, where L_0 is the lattice constant L at equilibrium.

$$\frac{L}{L_0} = \sigma \tag{5}$$

We applied the strains biaxially throughout the current work, so the surface lattice constant along the $[\overline{1}1\overline{2}]$ and $[\overline{1}10]$ directions was changed by the same fractional amount when strain was applied to surface FCC (111) simulations. All atoms in each strained slab were allowed to fully relax, except for the central atomic layers. Each Pt(111) simulation had 6 Pt layers, whilst each alloy simulation had 7 layers of Pt_3Ni or $PtNi_3$ alloy with further Ni and Pt layers—detailed later in the text—on each side of the slab. Subsequent slabs were separated by a vacuum with a width of approximately ten interplanar distances. For bulk simulations, the strains were applied identically and simultaneously along the [100], [010] and [001] directions. In the bulk case, however, no subsequent relaxation was considered.

To simulate the adsorption of atoms, the slabs were patterned symmetrically by attaching adsorbate atoms—either oxygen or hydrogen—in the same binding position on either side of a symmetric slab. The adsorption energy of E_{ads} was then defined as

$$E_{ads} = \frac{1}{2}(E_{A/S} - E_S - 2E_A) = \sigma \tag{6}$$

where $E_{A/S}$ is the Kohn–Sham energy of the adsorbate patterned slab, E_S is the energy of the unpatterned slab and E_A is the energy of the adsorbate. The factors of 2 and $1/2$ account for the patterning by adsorbates on both faces of the slab. Symmetric slabs were used throughout the current—with one minor exception, which is discussed in the text. This means that all quantitative outcomes were calculated using slabs which were either entirely unreacted or which were reacted identically adsorbate on either face. (3×3) and (2×2) surface unit cells were used to simulate the reacted Pt(111), and the $Pt/Ni/Pt_3Ni$-(111) and $Pt/Ni/PtNi_3$-(111) surfaces, respectively.

3. Results and Discussion

This section is structured in the following way: first, the bulk Pt and unreacted Pt(111) surface are investigated comparatively using the LDA and GGA exchange correlation functionals before investigating the reactivity of the Pt(111) surface towards oxygen and hydrogen. A similar methodology is then performed to investigate the more complex $Pt/Ni/Pt_3Ni$-(111) and $Pt/Ni/PtNi_3$-(111) surfaces before investigating their reactivity towards oxygen and hydrogen. The effects of adsorption on these surfaces are discussed with some particular focus on the magnetisation of the various surface, the origins of this magnetisation and the effects of adsorption on the magnetisation.

3.1. Unreacted Bulk Pt and Pt(111)

The orthogonal unit cell of the bulk FCC Pt crystal is shown in Figure 1.
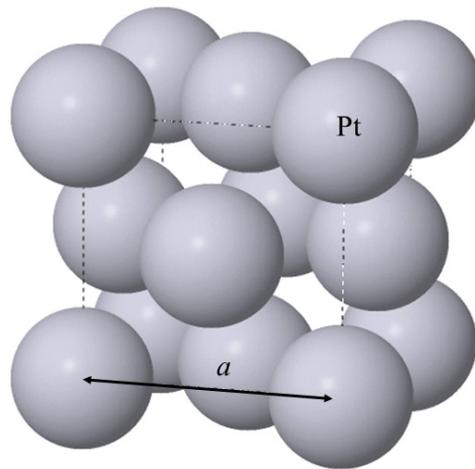
Figure 1. Orthogonal unit cell of the face-centred cubic (FCC) bulk Pt. The lattice parameter *a* is indicated by the solid arrow. The dashed lines are the edges of the orthogonal unit cell.

To determine the equilibrium lattice parameter *a*, the cohesive energy E_{coh} of the unit cell was calculated at different strains σ. The resulting equations of state are shown in Figure 2 and were calculated using the LDA and GGA approximations. The equilibrium lattice spacing occurs at the minimum of these curves.
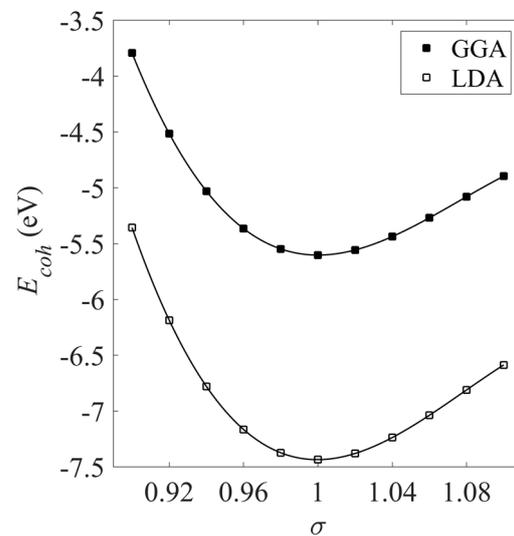

Figure 2. Cohesive energy E_{coh} of the bulk Pt crystal estimated using both the LDA and GGA estimates of the exchange-correlation.

Table 1 summarizes the bulk lattice parameters, equilibrium cohesive energies and magnetic moments for both the bulk Pt system (shown in Figure 1) and for the bulk Ni system, which has the same FCC structure as Pt. It can be seen from Table 1 that the LDA tends to underestimate the bond lengths compared to the experimental values. To compensate for this, the GGA estimates a lower cohesive energy compared to the LDA cohesive energies, and this can be seen in Figure 1. This lower estimation of the energy predicts longer equilibrium bond lengths for the GGA in Table 1.

Figure 3 shows the (a) Pt(111) surface and (b) the same slab in cross-sectional view. When strain is applied to the surface, the lattice constant along both the orthogonal

$[\overline{1}12]$ and $[\overline{1}10]$ directions was changed by the same fractional amount. Once this strain was applied, the atoms within the slab could relax freely, except for the central two layers which were constrained.

Table 1. The bulk lattice parameters a, cohesive energies E_{coh} and magnetic moments μ_{Pt} and μ_{Ni} for the bulk Ni and Pt metals. Cohesive energies are at the minima in the equations of state shown in Figure 2. The 'Theory/Experiment' column shows the exchange-correlation functional used (LDA/GGA) in the case of theoretical estimates of each of the physical parameter or shows the experimental value ('Exptl') where available.

| Metal	Theory/Experiment	a (Å)	E_{coh} (eV)	μ_{Pt} (μ_B)	μ_{Ni} (μ_B)
Pt	LDA	3.890	−7.141	0.000	-
	GGA	3.962	−5.586	0.000	-
	Exptl	3.912			-
Ni	LDA	3.427	−6.125	-	0.694
	GGA	3.518	−4.927	-	0.699
	Exptl	3.508		-	
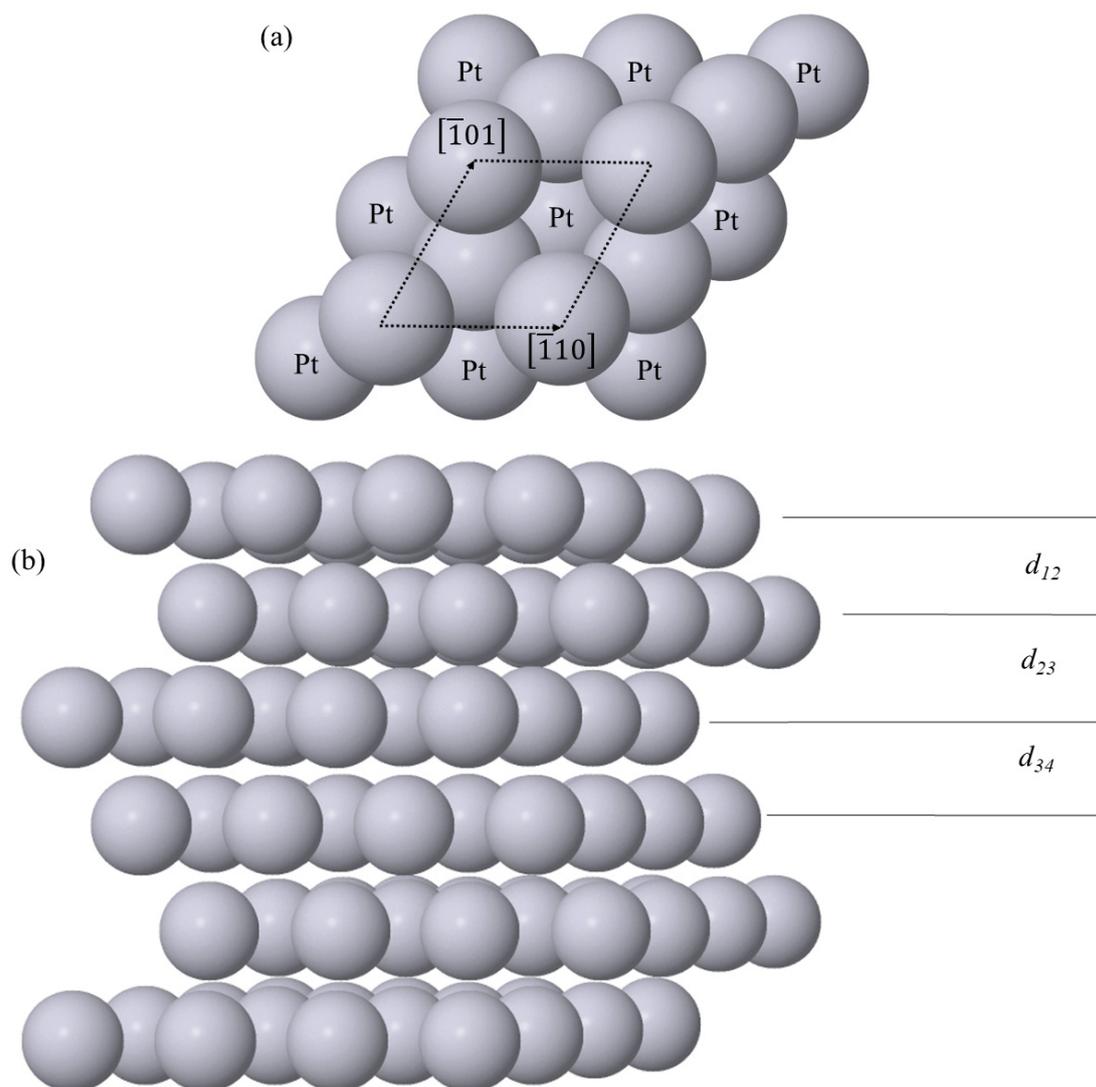
Figure 3. Structure of the (**a**) surface and (**b**) cross-section of Pt(111). In the latter, d_{12}, d_{23} and d_{34} are the surface-second layer, second-third layer and third-fourth layer spacings, respectively.

The resulting surface energies and layer spacings are shown in Figures 4 and 5, respectively. E_{surf} is overestimated by the LDA in the same way that the LDA cohesive energies were overestimated in Figure 2, with the GGA reducing the overestimation in both cases.
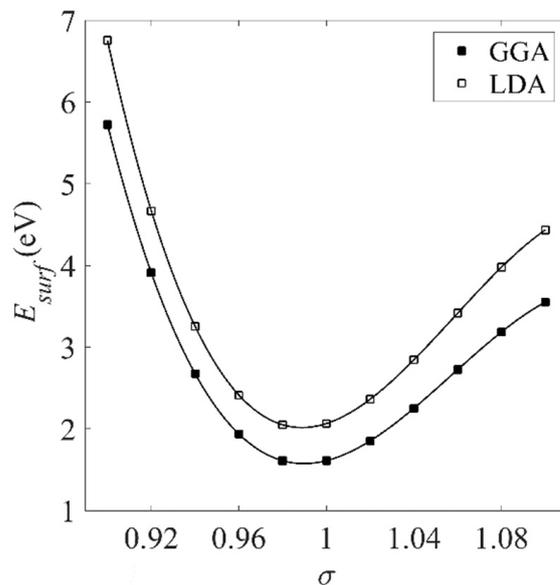

Figure 4. Surface energy E_{surf} of unreacted Pt(111) estimated using both the LDA and GGA exchange-correlation functionals.
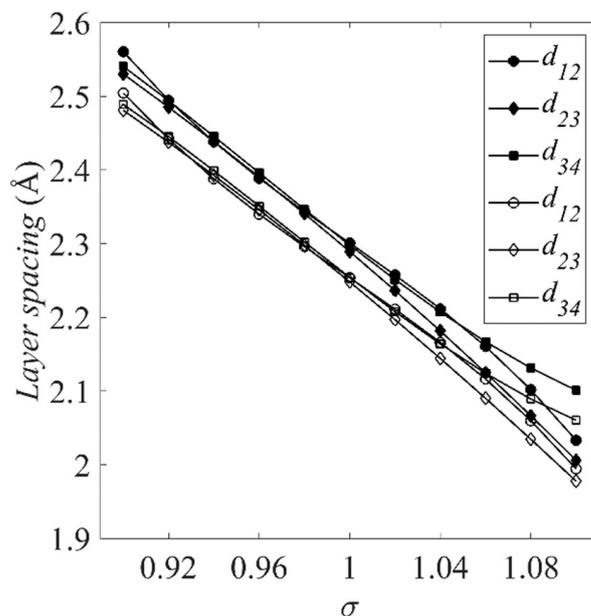

Figure 5. Layer spacings of the clean Pt(111) slab shown in Figure 3b. The filled (solid) symbols correspond to results obtained using the GGA; the unfilled (clear) symbols correspond to those obtained using the LDA.

Figure 5 shows the layer spacings for the Pt(111) slab defined in Figure 3. For $\sigma < 1.02$, the GGA estimates larger layer spacings.

The results and analysis in this section have so far focused on the energetic and the structural character of the bulk and unreacted pure metal surfaces. In order to develop the description of these systems, the projected density of states is now considered. Following

Equations (3) and (4) in the 'Computational Methods' section, the key metrics which will be used in the current work are the centre E_c and width w of the density of states. Figure 6 shows explicitly how these quantities develop for bulk Pt. The centre of both the d and the sp bands approaches the Fermi level as the strain σ increases, i.e., as the atoms in the bulk become increasingly separated. Accompanying this shift in E_c, the width w narrows. These two phenomena can be interpreted as the atoms approaching a more gas-like state as σ increases and are indicative that over the range of strains considered for the bulk Pt phase, a structural or electronic phase transition might not ordinarily be expected.
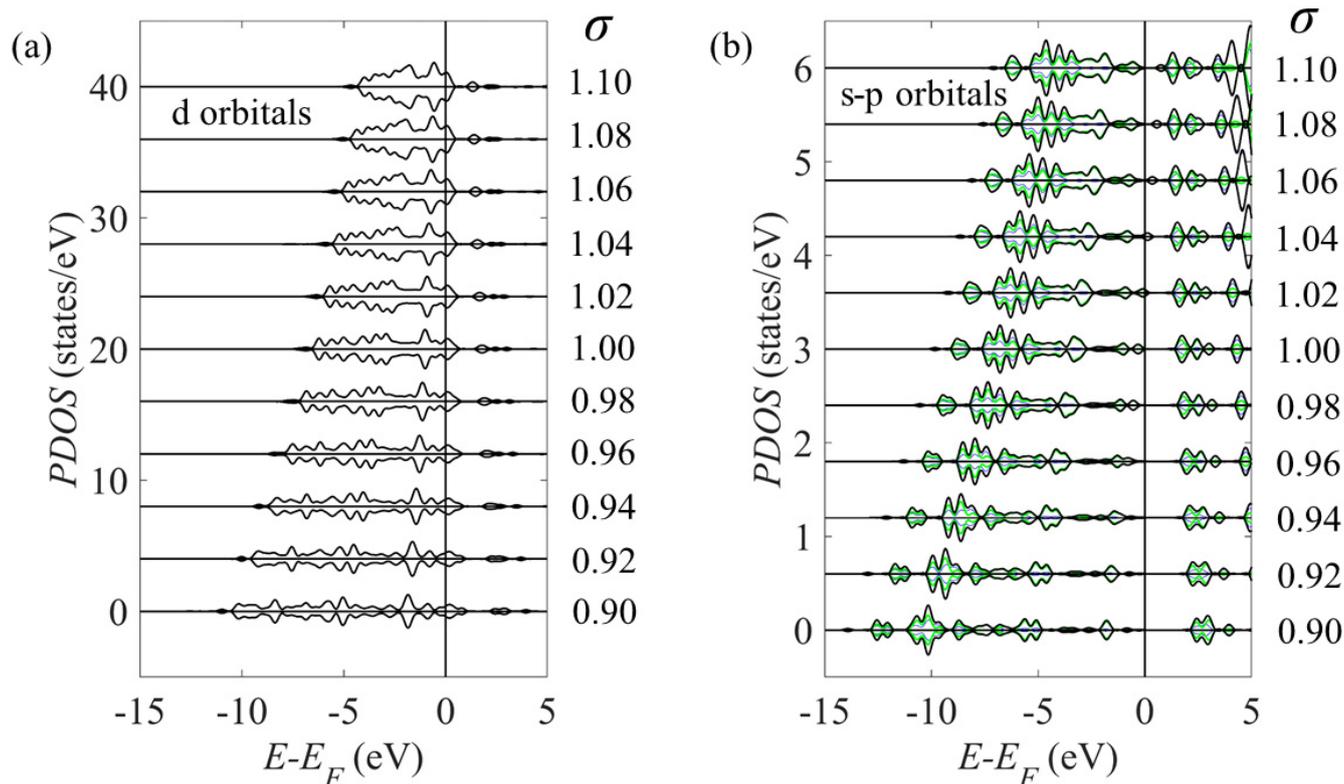

Figure 6. Projected density of states (PDOS) of the (**a**) d and (**b**) s-p orbitals for strained bulk Pt. The thin blue and green lines in (**b**) are the s and p PDOS, respectively, and the thick black line is the sum of the s and p PDOS. Each panel shows the spin up and down components as positive and negative curves, respectively. Subsequent curves are offset vertically for clarity and correspond to different amounts of strain σ.

Figure 7 shows the surface projected density of states (PDOS) in a strained Pt(111) slab at strains which correspond to the surface lattice constants of (111)-Pt_3Ni and $PtNi_3$ and shows little evidence that the surface Pt atoms become magnetised simply due to strain alone.

The layer-wise variation in the centre E_c and width w of the density of states under strain is summarized in Figure 8 which shows that the surface Pt E_c approach the Fermi level as strain becomes increasingly tensile and the distance between the atoms becomes greater. This effect is largely independent of the functional. For the deeper level atoms, the effect is only apparent for the more directional d bonds. The sp band is less directional, containing the diffuse s electrons which are less sensitive to the changes in the lattice constant. This is evidenced in the small gradient of the second and deeper layer atoms in Figure 8b.

(a)

(b)

$\sigma = 0.980$

(c)

(d)

$\sigma = 0.924$
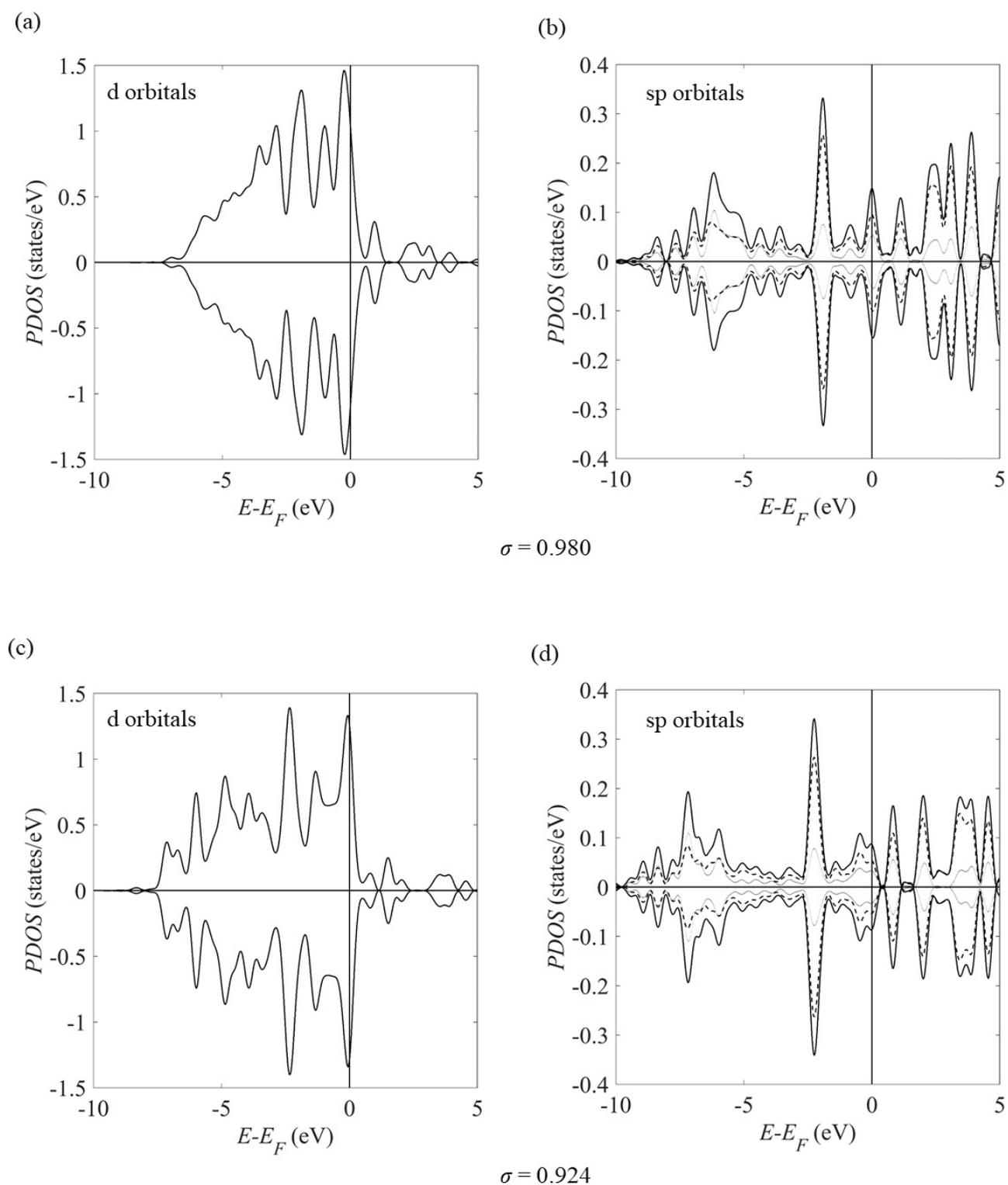
Figure 7. Projected density of states (PDOS) of the surface Pt atoms in a strained Pt(111) slab. The strains σ correspond to the strain in the Pt surface on a (**a**,**b**) Pt/Ni/Pt$_3$Ni and (**c**,**d**) Pt/Ni/PtNi$_3$ alloy. The sp orbitals panels (**b**,**d**) show the s, p and the sum of the s and p PDOS as thin dotted, dashed and thick solid curves, respectively. Each graph shows the spin up and down components as positive and negative curves, respectively.
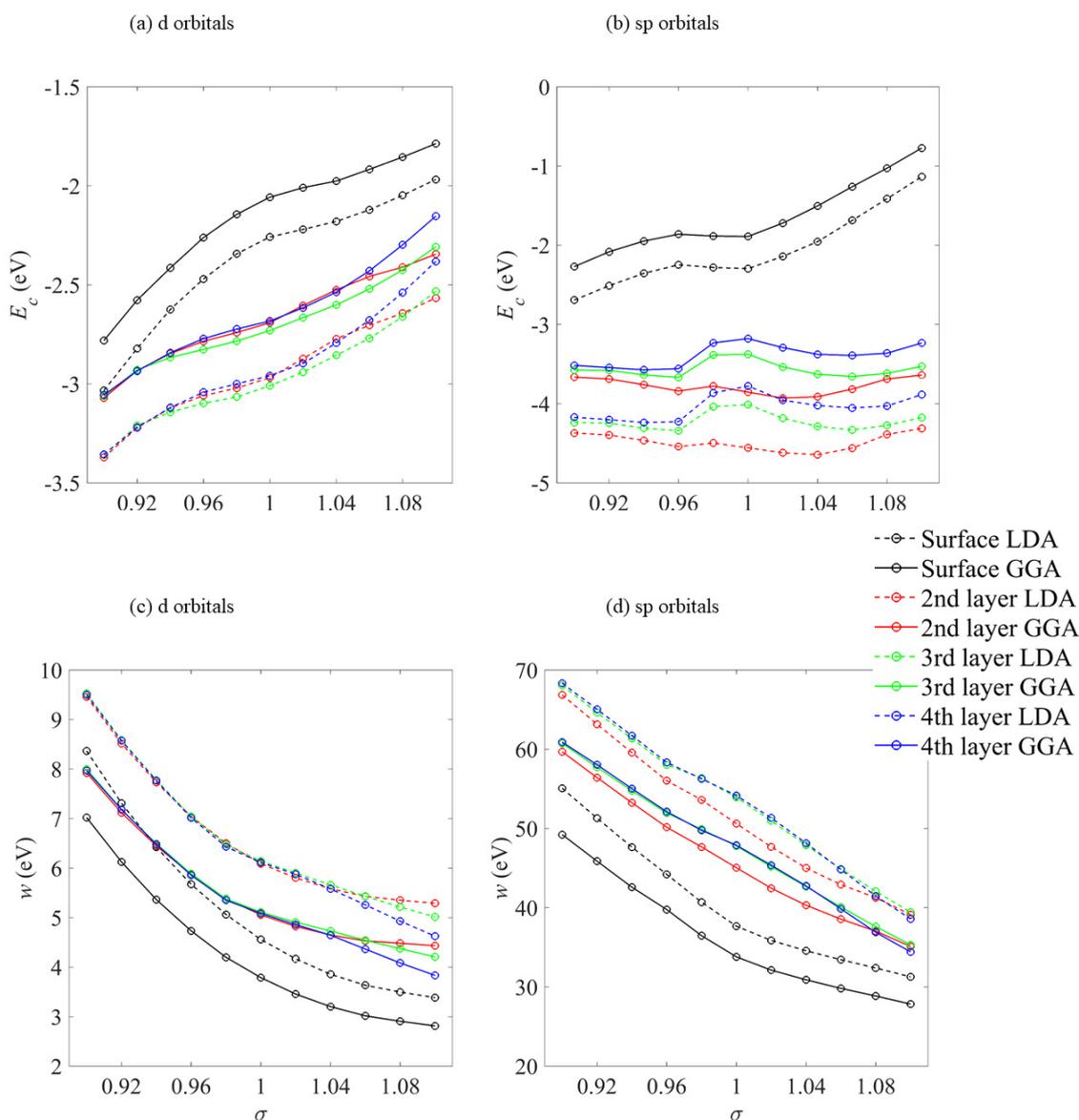
Figure 8. Layer-resolved band centre E_c and width w for the d and sp bands on an 7-layer Pt(111) slab. The dashed (solid) lines correspond to estimates made using the LDA (GGA) exchange-correlation functional.

3.2. Reacted Pt(111)

In the previous section, the energetic, structural, magnetic and electronic character of the Pt(111) surface under strain was presented. In the current section, the consequences of this character will be demonstrated in the response of the surface to oxygen and hydrogen.

Figure 9 shows the high-symmetry binding positions on the Pt(111) surface together with the (3 × 3) unit cell used in the current simulations. Figure 10 shows the adsorption energy under strain σ for (3 × 3)-O/Pt(111) and (3 × 3)-H/Pt(111). The oxygen atoms are seen to preferentially occupy the FCC sites for all strains. This observation is different from previous simulations [28], which showed that for compressive strains ($\sigma < 0.97$), the oxygen atoms preferentially occupy a bridge site. However, these earlier studies used a smaller (2 × 2) surface unit cell and observed a reconstruction of the surface, particularly for the related case of hydroxyl adsorption. This reconstruction does lead to a lower energy binding position—the values of E_{ads} in the earlier work are noted to be of the order of 0.5 eV lower than those in the current work. Consequentially, oxygen adsorption on strained Pt(111) should be considered in low coverage (current work) and high coverage regimes. The interactions in the high coverage

regime are not fully characterized, but the current evidence does suggest that lateral O-Pt interactions are significant.
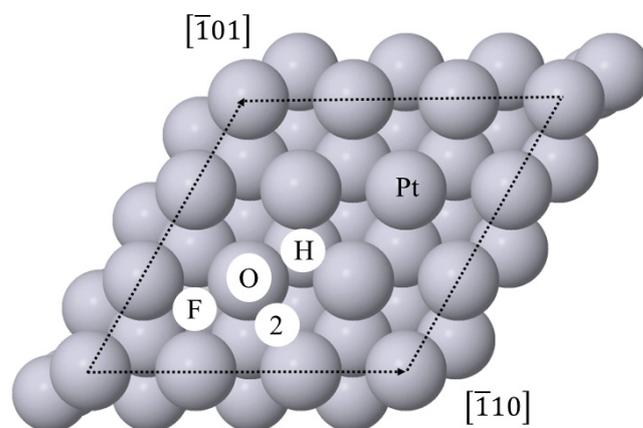

Figure 9. The 'O' on-top, 'F' FCC, 'H' HCP and '2' two-fold bridge high-symmetry binding positions on the Pt(111) surface. The dashed lines show the (3×3) surface unit cell used in the current simulations.

To provide a direct quantitative comparison between oxygen and hydrogen adsorption on the strained Pt(111) surface considered in the current section and adsorption on the alloy-based surfaces considered later in this work, Table 2 shows the adsorption energy E_{ads} for the unstrained ($\sigma = 1$) and compressively strained surfaces. The results in this table are consistent with those seen earlier in the current work—for example, in Figures 2 and 4—where the LDA is seen to overbind and consequently predict larger E_{ads}. The results in Table 2, more importantly, can be used to discuss the error in this energy, which arises from the choice of functional. Generally, oxygen is more tightly bound to the Pt(111) surface independent of the strain state.

Table 2. Oxygen and hydrogen adsorption energies on strained Pt(111). The rightmost column sub-headings ('LDA'/'GGA') indicate the exchange-correlation functional used. The strains used are those estimated within a Pt surface layer formed on a Pt$_3$Ni alloy (0.980/0.978) using the GGA and LDA approximations, respectively, and similarly (0.924/0.918) for a PtNi$_3$ alloy. All energies are in eV.

Binding Position	Strain σ	O/Pt(111)		H/Pt(111)	
		LDA	**GGA**	**LDA**	**GGA**
On-top	1.000	−2.895	−2.263	−2.416	−1.589
	0.980	-	−2.168	-	−1.586
	0.978	−2.773	-	−2.400	-
	0.924	-	−3.760	-	−2.976
	0.918	−4.842	-	−4.283	-
FCC	1.000	−3.913	−3.100	−2.426	−1.547
	0.980	-	−2.996	-	−1.519
	0.978	−3.780	-	−2.380	-
	0.924	-	−4.313	-	−2.906
	0.918	−5.622	-	−4.2664	-
HCP	1.000	−4.159	−3.278	−2.440	−1.547
	0.980	-	−3.146	-	−1.513
	0.978	−3.989	-	−2.387	-
	0.924	-	−4.286	-	−2.807
	0.918	−5.666	-	−4.161	-
2-fold	1.000	−4.596	−3.692	−2.467	−1.579
	0.980	-	−3.541	-	−1.535
	0.978	−4.402	-	−2.403	-
	0.924	-	−4.666	-	−2.818
	0.918	−6.027	-	−4.188	-
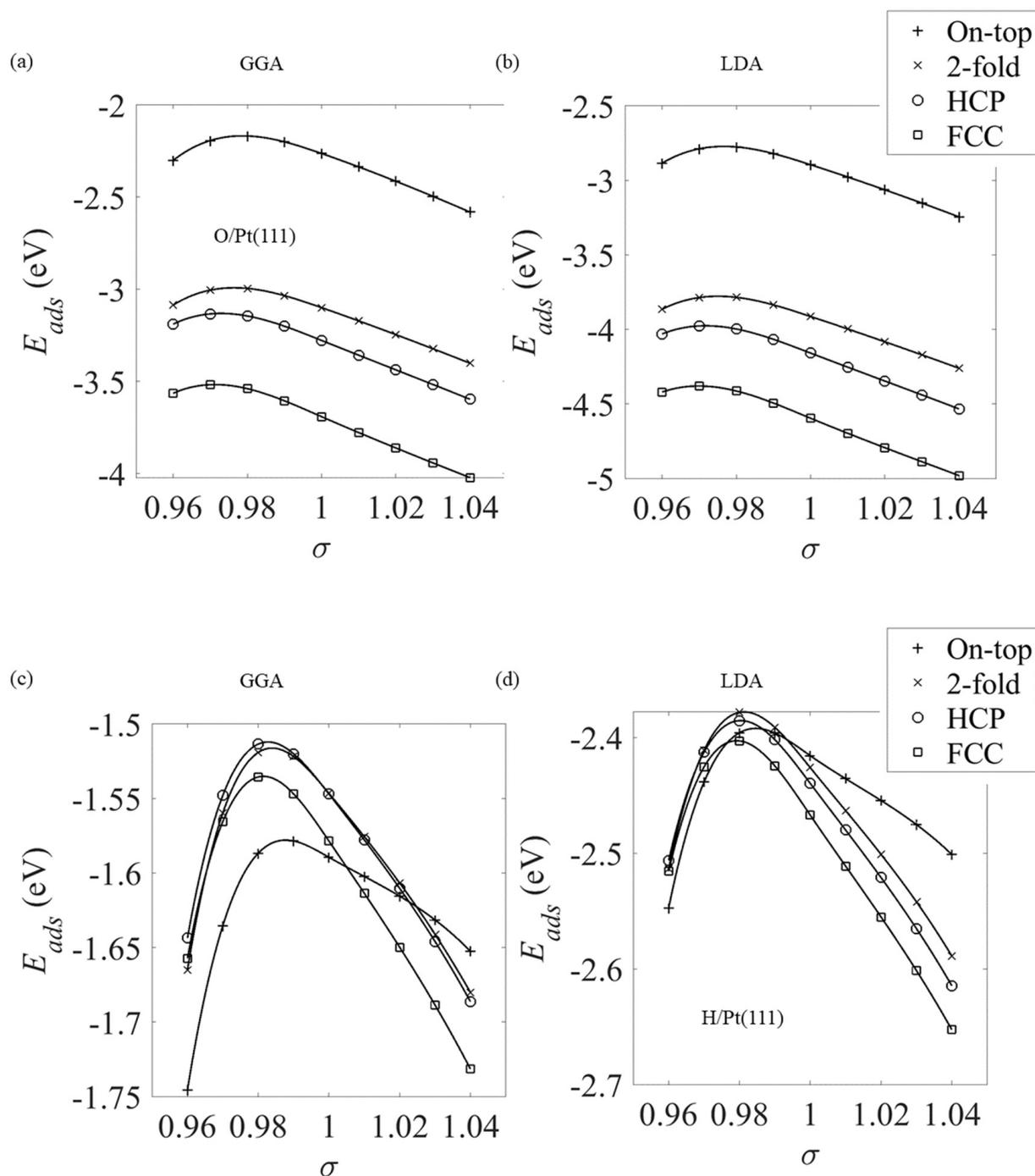
Figure 10. The binding energy of (**a**,**b**) oxygen and (**c**,**d**) hydrogen to the on-top, FCC, HCP and two-fold bridge high-symmetry binding positions on the Pt(111) surface as a function of strain σ. The curves were obtained using the (**a**,**c**) GGA and (**b**,**d**) LDA estimates of the exchange-correlation.

3.3. Unreacted Pt_xNi_{1-x} and $Pt/Ni/Pt_xNi_{1-x}$

Thus far, the results in the current work have focused on pure Pt in either bulk or slab form. This section now investigates the unreacted Pt_3Ni and $PtNi_3$ alloys in both bulk and slab form. Figure 11 shows the bulk unit cells of these alloys.
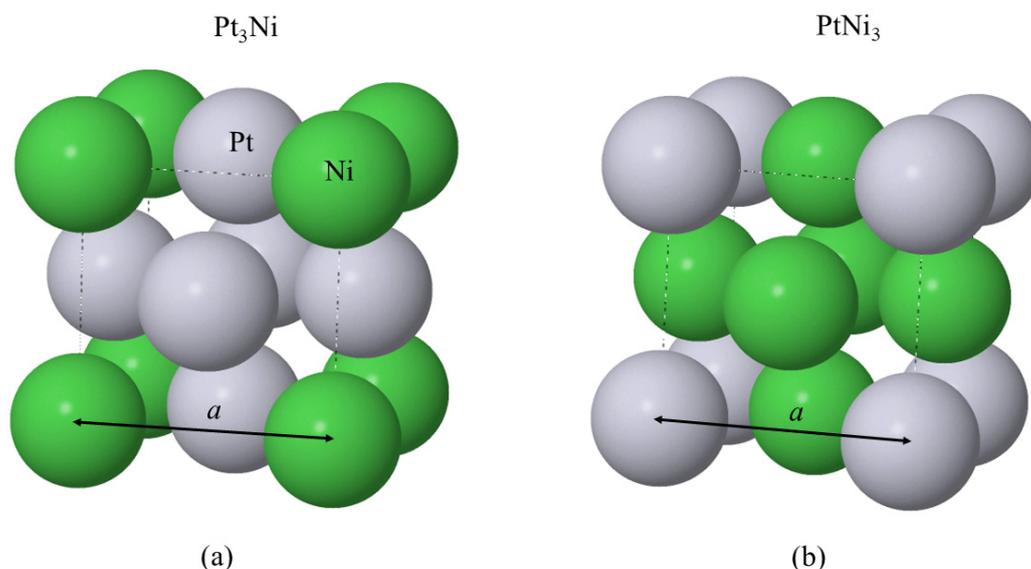
Figure 11. Orthogonal unit cell of the bulk (**a**) Pt_3Ni and (**b**) $PtNi_3$ (L1$_2$) structures. The lattice parameter *a* for both alloys is shown by the solid arrows. Dashed lines are the edges of the orthogonal unit cell. The Pt (Ni) atoms are shown as grey (green) spheres.

Table 3 shows the equilibrium lattice parameters, cohesive energies and magnetic moments for both unit cells. The Pt atoms can be seen to have developed a permanent magnetic moment in the presence of Ni, which is particularly noticeable for the $PtNi_3$ alloy.

Table 3. The bulk lattice parameters *a*, cohesive energies E_{coh} and magnetic moments μ_{Pt} and μ_{Ni} for the Pt_3Ni and $PtNi_3$. The 'Theory/Experiment' column shows the exchange-correlation functional used (LDA/GGA) in the case of theoretical estimates of each of the physical parameters or shows the experimental value ('Exptl') where available.

Alloy	Theory/ Experiment	a (Å)	E_{coh} (eV)	μ_{Pt} (μ_B)	μ_{Ni} (μ_B)
Pt_3Ni (L1$_2$)	LDA	3.805	−27.357	0.103	0.517
	GGA	3.884	−21.595	0.173	0.721
	Exptl [34]	3.836			
$PtNi_3$ (L1$_2$)	LDA	3.570	−25.533	0.290	0.584
	GGA	3.662	−20.470	0.373	0.806
	Exptl [34]	3.645			

Using the bulk lattice parameters presented in Table 3, the surfaces of unreacted (111)-$Pt/Ni/Pt_3Ni$ and (111)-$Pt/Ni/PtNi_3$ were fully relaxed. Based on the experimental studies of these systems [29], a Ni selvedge layer is set beneath the surface Pt layer. However, because of the complexity of the bulk alloy phase, the surface and selvedge layers are comprised of non-equivalent atoms. This is show in Figure 12a,b, where a subscript notation is adopted to identify the different types of surface and second layer Pt and Ni atom.
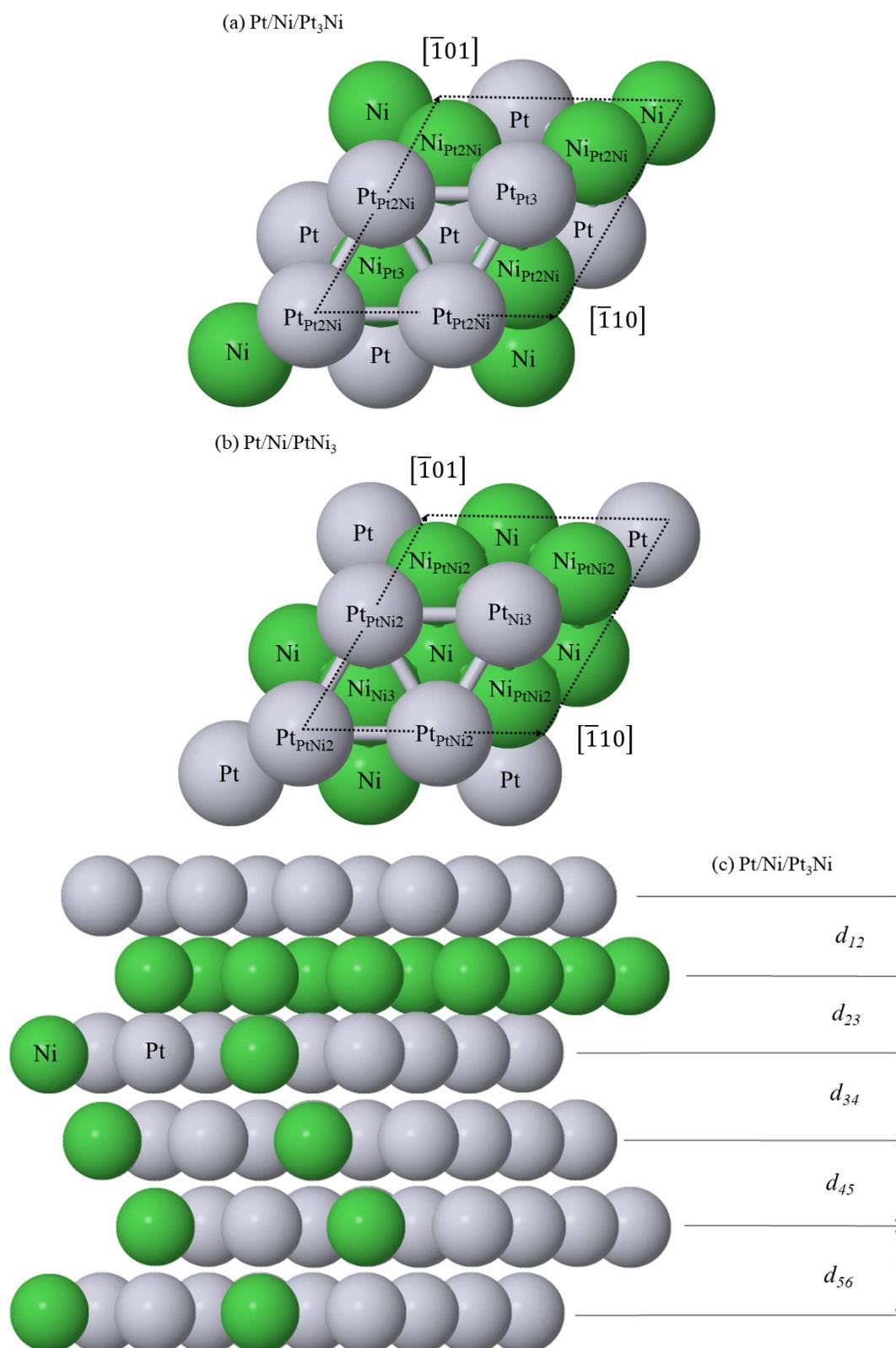
Figure 12. Structure of the surfaces of unreacted (**a**) (111)-Pt/Ni/Pt$_3$Ni and (**b**) (111)-Pt/Ni/PtNi$_3$ and (**c**) the cross-section of unreacted (111)-Pt/Ni/Pt$_3$Ni. In the latter, d_{12}, d_{23}, d_{34}, d_{45} and d_{56} are interlayer spacings. In (**a**,**b**), the third layer Pt and Ni atoms are labelled by their unannotated chemical symbol, whereas the surface Pt and second layer Ni atoms carry a subscript which is the stoichiometry of their nearest third layer neighbours. This stoichiometry gives rise to non-equivalent on-top, FCC and HCP surface binding positions and three non-equivalent 2-fold bridge sites.

Table 4 summarizes the interlayer spacing for the alloy systems. The variation in height between the different surface Pt and second layer Ni species is averaged across each layer.

Table 4. The interlayer spacing d_{12}, d_{23}, d_{34}, d_{45} and d_{56} defined in Figure 12 of the unreacted (111)-Pt/Ni/Pt$_3$Ni and (111)-Pt/Ni/PtNi$_3$ surfaces. The 'Functional' column shows the exchange-correlation functional used (LDA/GGA). All lengths are given in units of Å.

Alloy	Functional	d_{12}	d_{23}	d_{34}	d_{45}	d_{56}
Pt$_3$Ni (L1$_2$)	LDA	2.042	1.977	2.226	2.217	2.207
	GGA	2.090	2.034	2.285	2.269	2.259
PtNi$_3$ (L1$_2$)	LDA	2.155	1.984	2.084	2.081	2.073
	GGA	2.193	2.035	2.141	2.137	2.128

Figure 13 shows the planar-averaged spin density $\langle \rho_\uparrow - \rho_\downarrow \rangle$ for the clean (111)-Pt/Ni/Pt$_3$Ni and (111)-Pt/Ni/PtNi$_3$ slabs. Each slab is composed of 7 layers of alloy bounded by Ni selvedge and Pt surface layers, and the averaging is taken parallel to the (111) plane.
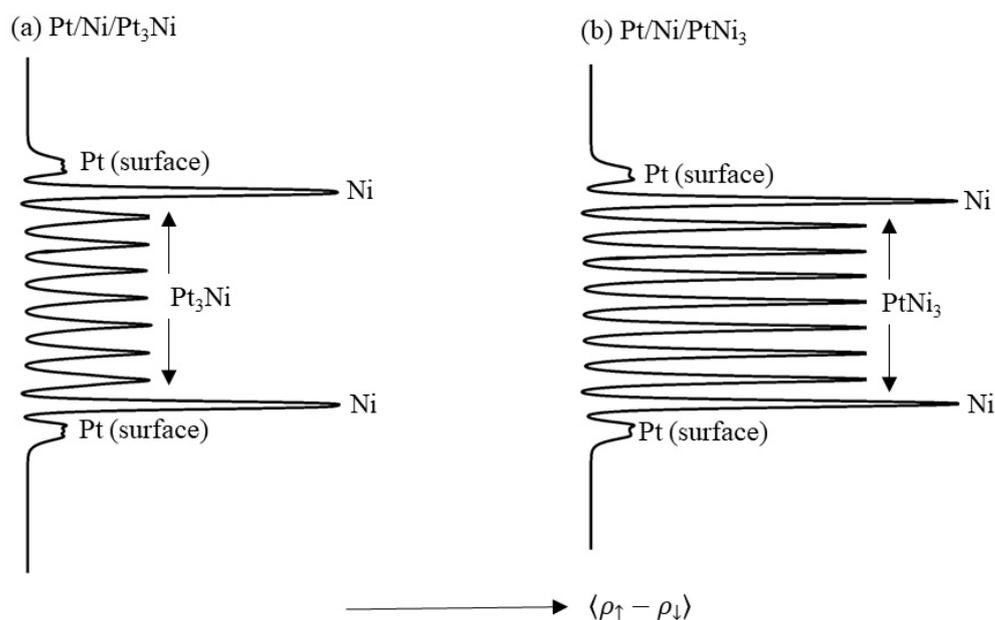

Figure 13. Average spin density $\langle \rho_\uparrow - \rho_\downarrow \rangle$ of the surfaces of unreacted (**a**) (111)-Pt/Ni/Pt$_3$Ni and (**b**) (111)-Pt/Ni/PtNi$_3$. The averaging was performed parallel to the (111) plane. The labels show the regions of bulk Pt$_3$Ni and PtNi$_3$, selvedge Ni and surface Pt in symmetric slabs, which each have 11 atomic layers in total.

Quantitatively, the Pt surface layer has an average spin polarization of 0.006 Å^{-1} for both slabs shown in Figure 13. The Ni second layer has an average spin polarization of 0.051 Å^{-1} and 0.061 Å^{-1} for the Pt$_3$Ni and PtNi$_3$ alloys, respectively. The values for the Ni atoms are consistent with the ferromagnetic moment that the Ni atoms carry. The induced magnetisation in the surface Pt layers is significant, particularly when it is compared to the negligible moment carried by the surface atoms in a pure Pt(111) slab, which was discussed earlier in this manuscript. The consequences of this induced moment in the surface Pt layer for the adsorption of oxygen and hydrogen and the effects of adsorption on this moment will be discussed in the next section.

3.4. Reacted Pt/Ni/Pt$_x$Ni$_{1-x}$

Figure 14 shows the high-symmetry binding positions on the (111)-Pt/Ni/Pt$_3$Ni surface. The binding positions on the (111)-Pt/Ni/PtNi$_3$ surface are identically arranged, though the Pt (Ni) atoms are replaced with Ni (Pt) atoms in the alloy layers.
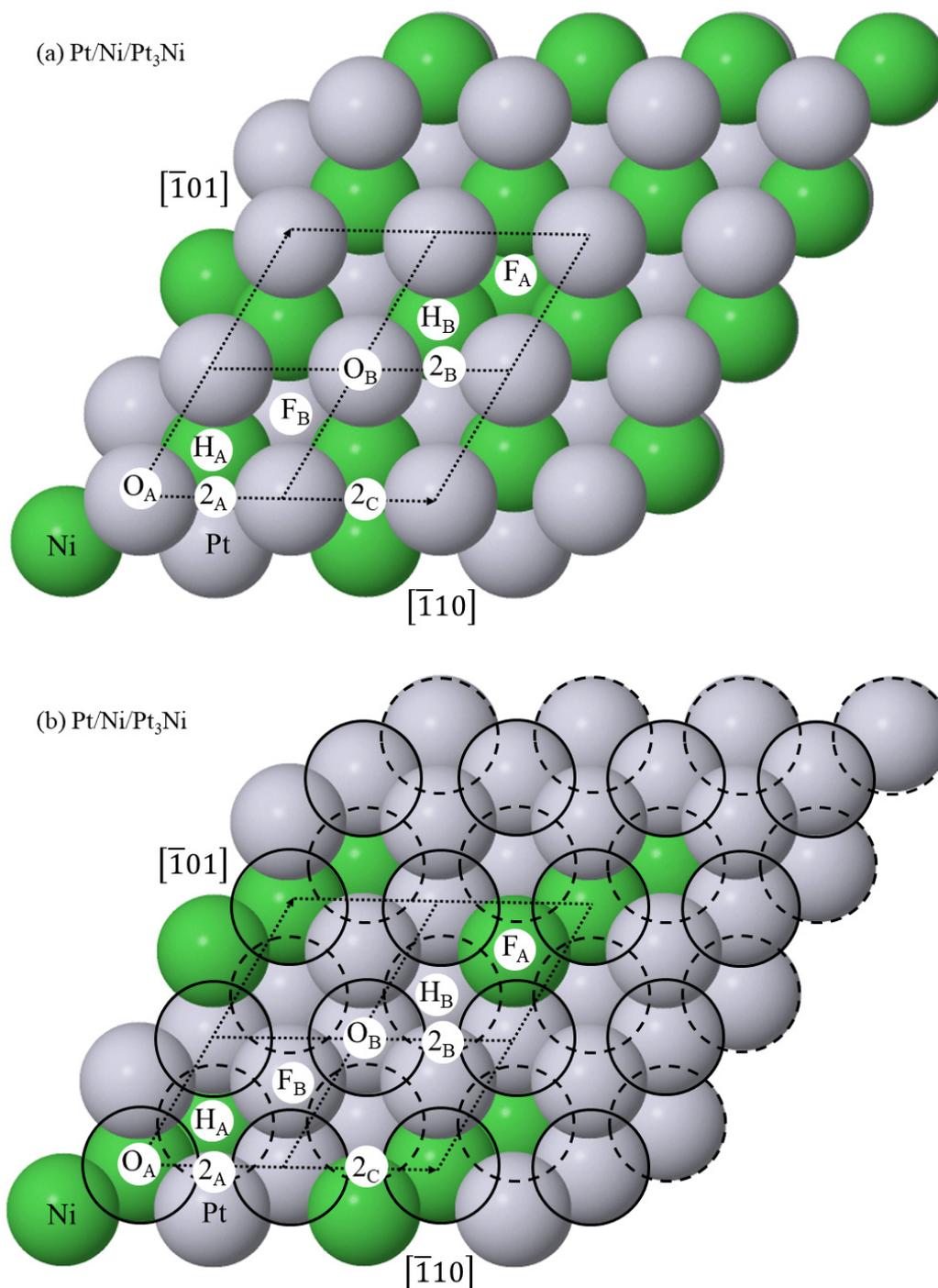
Figure 14. (**a**) The 'O$_A$' and 'O$_B$' on-top, 'F$_A$' and 'F$_B$' FCC, 'H$_A$' and 'H$_B$' HCP and '2$_A$', '2$_B$' and '2$_C$' two-fold bridge high-symmetry binding positions on the reacted Pt/Ni/Pt$_3$Ni-(111) surface. In (**b**), the surface and second layers—the pure Pt and Ni layers—are replaced with transparent circles bounded by solid and dashed lines, respectively. The straight dotted lines show the (2 × 2) surface unit cell used in the current simulations. The Pt/Ni/PtNi$_3$-(111) is generated by changing every Pt (Ni) atom in layer 3 and deeper for a Ni (Pt) atom.

Table 5 shows the adsorption energies E_{ads} at the high symmetry sites for oxygen and hydrogen. These energies can be compared directly with the adsorption energies for the strained Pt(111) surface presented in Table 2. For oxygen adsorption, the adsorption energies are between 0.176 and 1.081 eV greater on the (111)-Pt/Ni/Pt$_3$Ni surface than on the strained Pt(111) surface, across both functionals. This shows that a ligand effect exists on the (111)-Pt/Ni/Pt$_3$Ni surface which causes the oxygen atoms to bind more strongly to that surface than to the strained Pt(111) surface. Conversely, on the (111)-Pt/Ni/PtNi$_3$ surface, the adsorption energies are 0.863 to 1.874 eV lower than on the equivalently strained Pt(111) surface. The ligand effect does have some depth sensitivity. It does not depend on the nearest neighbour interactions between the adsorbate and the surface Pt atoms and does extend even beyond the second nearest-neighbour interactions involving the Ni atoms in the second (selvedge) layer. For hydrogen adsorption, a similar set of energy differences can be determined. The hydrogen atoms bind between 0.320 and 0.636 eV more strongly to the (111)-Pt/Ni/Pt$_3$Ni surface than to the strained Pt(111) surface, and between 0.897 and 1.437 eV less strongly to the (111)-Pt/Ni/PtNi$_3$ surface than to the strained Pt(111) surface.

Table 5. Oxygen and hydrogen adsorption energies E_{ads} on the high symmetry sites of the (111)-Pt/Ni/Pt$_3$Ni and (111)-Pt/Ni/PtNi$_3$ surfaces. The binding positions are defined in Figure 14. The column subheadings ('LDA'/'GGA') indicate the exchange-correlation functional used. The values shown in bold are the lowest energy for a particular type of binding position. All energies are in eV.

Binding Position		O/(111)-Pt/Ni/Pt$_3$Ni		O/(111)-Pt/Ni/PtNi$_3$	
		LDA	**GGA**	**LDA**	**GGA**
On-top	A	**−3.496**	**−2.782**	−3.382	**−2.672**
	B	−3.411	−2.701	**−3.390**	−2.668
FCC	A	−4.861	−3.805	−4.389	−3.422
	B	**−4.887**	**−3.825**	**−4.424**	**−3.450**
HCP	A	**−4.625**	**−3.589**	**−4.203**	−3.239
	B	−4.558	−3.526	−4.201	**−3.241**
2-fold	A	−4.332	−3.366	−4.102	−3.178
	B	**−4.578**	−3.328	**−4.153**	**−3.203**
	C	−4.337	**−3.356**	−4.067	−3.138
Binding Position		H/(111)-Pt/Ni/Pt$_3$Ni		H/(111)-Pt/Ni/PtNi$_3$	
		LDA	**GGA**	**LDA**	**GGA**
On-top	A	−2.833	−1.879	**−2.861**	**−1.919**
	B	**−2.867**	**−1.906**	−2.833	−1.881
FCC	A	−2.998	−1.992	−2.813	**−1.895**
	B	**−3.016**	**−2.010**	**−2.829**	−1.892
HCP	A	−2.988	−1.979	−2.835	**−1.910**
	B	**−2.997**	**−1.989**	**−2.848**	−1.908
2-fold	A	−2.940	−1.940	−2.859	**−1.911**
	B	**−2.952**	**−1.953**	**−2.875**	−1.908
	C	−2.947	−1.947	−2.846	−1.895

Table 6 compares the nearest-neighbour O-Pt and H-Pt bond lengths obtained using both the LDA and the GGA functionals. The LDA predicts shorter bond lengths than the GGA in almost all cases. This is indicative of a functional which is overestimating the bonding and therefore predicting shorter bond lengths than might be observed experimentally. Conversely the GGA tends to underestimate the binding and therefore predicts generally longer bond lengths. For these reasons, experimentalists might anticipate measuring a bond length between the LDA and GGA values presented in this table.

The next step in characterizing the oxygen and hydrogen adsorption is to look in more detail at the density of states of the adsorbate and substrate for the alloy-bearing systems, in the same way that these quantities were analysed for the Pt(111) systems earlier in this work. Table 7 shows the first and second moments of the surface Pt atoms for these systems. As the surface Pt atoms in the strained Pt(111) are not magnetised, both the centre and width of the spin up and down components are identical, so only one value is quoted for each for Pt(111). For both alloys, the width of the spin polarized d-band orbital is larger than the equivalent width for the strained Pt(111). However, the behaviour of the centre of the d-band is less clearly defined. For the Pt/Ni/Pt$_3$Ni, the $E_{c;Pt}$ are close to the $E_{c\downarrow}$ values for both the LDA and GGA simulations. This result is surprising within the conventional d-band model, as it was noted earlier in this section that comparisons of the adsorption energy between the Pt/Ni/Pt$_3$Ni and strained Pt(111) varied significantly with the density functional. For Pt/Ni/PtNi$_3$, the situations appear more consistent with the d-band model, as there is some variation in the $E_{c;Pt}$ and the $E_{c\uparrow}$ and $E_{c\downarrow}$ for both the LDA and GGA simulations, with the $E_{c;Pt}$ changing alignment with the functional, which is more consistent with the d-band model.

Table 6. Nearest-neighbour oxygen-Pt and hydrogen-Pt bond lengths on the high symmetry sites of the (111)-Pt/Ni/Pt$_3$Ni and (111)-Pt/Ni/PtNi$_3$ surfaces. All the nearest-neighbour Pt atoms lie in the surface Pt layer. The binding positions are defined in Figure 14. The column subheadings ('LDA'/'GGA') indicate the exchange-correlation functional used. All bond lengths are in Å.

Binding Position		O/(111)-Pt/Ni/Pt$_3$Ni		O/(111)-Pt/Ni/PtNi$_3$	
		LDA	GGA	LDA	GGA
On-top	A	1.83	1.86	1.78	1.80
	B	1.84	1.86	1.80	1.80
FCC	A	2.03	2.07	2.04	2.07
	B	2.04	2.07	2.05	2.09
HCP	A	2.04	2.07	2.05	2.09
	B	2.04	2.07	2.06	2.10
2-fold	A	1.98	2.01	1.98	2.01
	B	2.02	2.02	1.97	2.02
	C	1.98	2.02	1.98	2.02
Binding Position		H/(111)-Pt/Ni/Pt$_3$Ni		H/(111)-Pt/Ni/PtNi$_3$	
		LDA	GGA	LDA	GGA
On-top	A	1.57	1.58	1.56	1.56
	B	1.57	1.57	1.56	1.56
FCC	A	1.83	1.85	1.79	1.81
	B	1.85	1.85	1.88	1.87
HCP	A	1.85	1.86	1.81	1.86
	B	1.86	1.87	1.83	1.86
2-fold	A	1.75	1.76	1.73	1.74
	B	1.77	1.77	1.77	1.78
	C	1.76	1.77	1.76	1.77

Table 7. The spin-resolved first and second moments of the d-band of the surface Pt atoms in the Pt_3Ni and $PtNi_3$ alloy-bearing systems and in the surface Pt atoms in strained Pt(111). The up and down arrows denote the spin up and down components of the surface Pt atoms in the alloy systems, and 'Pt' denotes the surface Pt atoms in strained Pt(111). The number in brackets after the $E_{c;Pt}$ and w_{Pt} is the strain σ at which the quantity was determined. The 'Functional' column shows the exchange-correlation functional used (LDA/GGA). All the band centers are relative to the Fermi energy; all the energies and widths are in eV.

Alloy	Functional	$E_{c\uparrow}$	$E_{c\downarrow}$	$E_{c;Pt}$	$w_\uparrow$	$w_\downarrow$	w_{Pt}
Pt/Ni/Pt$_3$Ni (L1$_2$)	LDA	−2.439	−2.330	−2.343 (0.9781)	8.046	8.155	5.211 (0.9781)
	GGA	−2.313	−2.161	−2.144 (0.9803)	6.803	6.987	4.199 (0.9803)
Pt/Ni/PtNi$_3$ (L1$_2$)	LDA	−2.837	−2.724	−2.846 (0.9177)	10.597	10.721	4.510 (0.9177)
	GGA	−2.567	−2.418	−2.380 (0.9243)	8.787	8.978	3.670 (0.92428)

A further observation is that the magnetisation of the surface Pt atoms is generally reduced by both oxygen and hydrogen adsorption. This is shown qualitatively in Figure 15, where the surface average spin moment of the Pt atoms in the reacted surface is less than that on the clean surface.
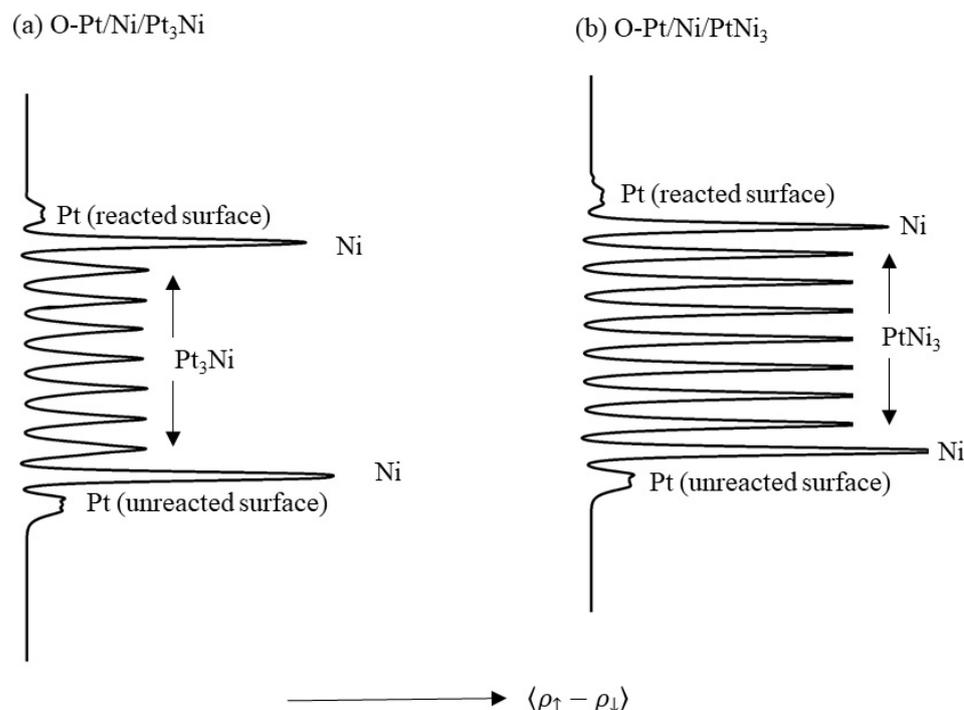

Figure 15. Average spin density $\langle \rho_\uparrow - \rho_\downarrow \rangle$ of the surfaces of (**a**) O-Pt/Ni/Pt$_3$Ni(111) and (**b**) O-Pt/Ni/PtNi$_3$(111). The oxygen atoms are bound in the FCC 'A' ('FA') sites defined in Figure 14 in the upper 'reacted' surfaces, whilst the lower surface is unreacted. This asymmetry is simply intended to highlight the change in the magnetic character of the respective surface Pt layers during adsorption, and quantitative results from these simulations were not subsequently used in this work. The averaging was performed parallel to the (111) plane. The labels show the regions of bulk Pt$_3$Ni and PtNi$_3$, selvedge Ni and surface Pt.

The observation that the magnetisation of the surface Pt atoms is reduced by both oxygen and hydrogen adsorption is presented quantitatively in Table 8. Comparing the reacted and unreacted surfaces, the adsorption generally reduces the surface Pt atoms moment by up to 75%. This is not the case for on-top adsorption, however, where the magnetic moment is seen to increase.

Table 8. Magnetisation of the surface Pt atoms on the oxygen and hydrogen reacted and clean (111)-Pt/Ni/Pt$_3$Ni and (111)-Pt/Ni/PtNi$_3$ surfaces. For the reacted surfaces, the Pt atoms are the nearest neighbours to either the O or the H adsorbate. The binding positions are defined in Figure 14, and the column subheadings ('LDA'/'GGA') indicate the exchange-correlation functional used. The numbers in brackets shown are the magnetic moments of the adsorbate. All magnetic moments in these tables are in units of μ_B.

Binding Position		O/(111)-Pt/Ni/Pt$_3$Ni		O/(111)-Pt/Ni/PtNi$_3$	
		LDA	**GGA**	**LDA**	**GGA**
On-top	A	0.263 (0.575)	0.303 (0.641)	0.310 (0.543)	0.422 (0.649)
	B	0.257 (0.565)	0.321 (0.654)	0.251 (0.499)	0.403 (0.632)
FCC	A	0.049 (0.007)	0.068 (0.003)	0.028 (−0.008)	0.039 (−0.001)
	B	0.038 (−0.010)	0.047 (−0.020)	0.032 (0.004)	0.042 (0.008)
HCP	A	0.040 (−0.014)	0.074 (−0.014)	0.030 (−0.015)	0.056 (0.004)
	B	0.042 (−0.008)	0.073 (−0.002)	0.028 (−0.020)	0.051 (−0.003)
2-fold	A	0.052 (0.045)	0.095 (0.090)	0.026 (−0.004)	0.032 (0.013)
	B	0.037 (−0.004)	0.072 (0.040)	0.024 (0.007)	0.035 (0.025)
	C	0.133 (0.041)	0.186 (0.078)	0.069 (−0.007)	0.102 (0.016)
Unreacted	-	0.180	0.216	0.188	0.211
Binding Position		H/(111)-Pt/Ni/Pt$_3$Ni		H/(111)-Pt/Ni/PtNi$_3$	
		LDA	**GGA**	**LDA**	**GGA**
On-top	A	0.033 (−0.008)	0.035 (−0.015)	0.024 (−0.008)	0.028 (−0.012)
	B	0.034 (−0.010)	0.033 (−0.017)	0.025 (−0.007)	0.027 (−0.010)
FCC	A	0.072 (−0.001)	0.090 (−0.002)	0.063 (−0.001)	0.064 (−0.002)
	B	0.080 (−0.002)	0.088 (−0.003)	0.051 (−0.001)	0.061 (−0.003)
HCP	A	0.074 (−0.002)	0.093 (−0.003)	0.077 (−0.001)	0.071 (−0.002)
	B	0.081 (−0.002)	0.088 (−0.003)	0.054 (−0.001)	0.066 (−0.002)
2-fold	A	0.059 (−0.003)	0.073 (−0.005)	0.046 (−0.002)	0.051 (−0.004)
	B	0.065 (−0.003)	0.070 (−0.005)	0.045 (−0.002)	0.050 (−0.004)
	C	0.106 (−0.002)	0.116 (−0.004)	0.074 (−0.002)	0.089 (−0.004)

4. Conclusions

The reacted (111)-Pt/Ni/Pt$_3$Ni and (111)-Pt/Ni/PtNi$_3$ surfaces have been investigated using density functional theory (DFT). These investigations have focused on the binding energy, bond lengths, magnetisation and electronic density of states of adsorbates and the surface Pt atoms during the incorporation of oxygen and hydrogen into the high symmetry ad-sites.

The current work has shown that the surface Pt atoms in the unreacted (111)-Pt/Ni/Pt$_x$Ni$_{1-x}$ slabs are permanently magnetised. In comparison with appropriately strained clean Pt(111), this magnetisation has been seen to be due to a ligand effect between the surface Pt and the selvedge Ni atoms, instead of being seen as a geometric effect due to the strain.

The adsorption of oxygen and hydrogen into the high symmetry sites quenches this magnetisation. Comparing the adsorption energies of the reacted (111)-Pt/Ni/Pt$_x$Ni$_{1-x}$ slabs and the reacted, strained Pt(111) surface, it has been shown that this quenching of the magnetisation significantly increases the binding energy of the adsorbate. This effect has been shown to be predicted with both the LDA and the GGA.

A survey of the behaviour of the clean Pt(111) and bulk Pt systems has been included in the current work. This survey has quantified the shifting in the d- and sp-band centres and changes to the width of these bands under strain and has explained this behaviour using a simple bulk-to-gas phase model. The correlation between the adsorption energy of H/Pt(111) and O/Pt(111) under strain and the position of the centre of the d-band has been qualitatively discussed.

Institutional Review Board Statement: Not applicable.

Informed Consent Statement: Not applicable.

Data Availability Statement: Not applicable.

Conflicts of Interest: The author declares no conflict of interest.

References

1. Strasser, P.; Koh, S.; Anniyev, T.; Greeley, J.P.; More, K.; Yu, C.; Liu, Z.; Kaya, S.; Nordlund, D.; Ogasawara, H.; et al. Lattice-strain control of the activity in dealloyed core–shell fuel cell catalysts. *Nat. Chem.* **2010**, *2*, 454–460. [CrossRef] [PubMed]
2. Mavrikakis, M.; Hammer, B.; Nørskov, J.K. Effect of Strain on the Reactivity of Metal Surfaces. *Phys. Rev. Lett.* **1998**, *81*, 2819–2822. [CrossRef]
3. Wu, J.; Li, P.; Pan, Y.-T.F.; Warren, S.; Yin, X.; Yang, H. Surface lattice-engineered bimetallic nanoparticles and their catalytic properties. *Chem. Soc. Rev.* **2012**, *41*, 8066–8074. [CrossRef] [PubMed]
4. Hülsey, M.J.; Lim, C.W.; Yan, N. Promoting heterogeneous catalysis beyond catalyst design. *Chem. Sci.* **2020**, *11*, 1456–1468. [CrossRef]
5. Khorshidi, A.; Violet, J.; Hashemi, J.; Peterson, A.A. How strain can break the scaling relations of catalysis. *Nat. Catal.* **2018**, *1*, 263–268. [CrossRef]
6. Gan, L.; Yu, R.; Luo, J.; Cheng, Z.; Zhu, J. Lattice Strain Distributions in Individual Dealloyed Pt–Fe Catalyst Nanoparticles. *J. Phys. Chem. Lett.* **2012**, *3*, 934–938. [CrossRef] [PubMed]
7. Gamler, J.T.L.; Ashberry, H.M.; Sang, X.; Unocic, R.R.; Skrabalak, S.E. Building Random Alloy Surfaces from Intermetallic Seeds: A General Route to Strain-Engineered Electrocatalysts with High Durability. *ACS Appl. Nano Mater.* **2019**, *2*, 4538–4546. [CrossRef]
8. Lin, L.; Sun, Z.; Yao, H.; Yuan, M.; Yang, H.; Li, H.; Zhang, Q.; Wang, D.; Gu, L.; Sun, G.; et al. Tuning Surface Lattice Strain toward a Pt–Skin CoPtx Truncated Octahedron for Hydrogen Evolution Reaction. *J. Phys. Chem. C* **2019**, *123*, 29722–29728. [CrossRef]
9. Niu, Z.; Wan, Y.; Li, X.; Zhang, M.; Liu, B.; Chen, Z.; Lu, G.; Yan, K. In-situ regulation of formic acid oxidation via elastic strains. *J. Catal.* **2020**, *389*, 631–635. [CrossRef]
10. Wang, A.; Zhao, Z.; Hu, D.; Niu, J.; Zhang, M.; Yan, K.; Lu, G. Tuning the oxygen evolution reaction on a nickel–iron alloy via active straining. *Nanoscale* **2019**, *11*, 426–430. [CrossRef]
11. Liu, M.; Zhao, Z.; Duan, X.; Huang, Y. Nanoscale Structure Design for High-Performance Pt-Based ORR Catalysts. *Adv. Mater.* **2019**, *31*, e1802234. [CrossRef] [PubMed]
12. Xia, Z.; Guo, S. Strain engineering of metal-based nanomaterials for energy electrocatalysis. *Chem. Soc. Rev.* **2019**, *48*, 3265–3278. [CrossRef] [PubMed]
13. Callejas-Tovar, R.; Balbuena, P.B. Effect of Subsurface Vacancies on Oxygen Reduction Reaction Activity of Pt-Based Alloys. *J. Phys. Chem. C* **2012**, *116*, 14414–14422. [CrossRef]
14. Jagannath, M.S.P.; Divi, S.; Chatterjee, A. Kinetic Map for Destabilization of Pt-Skin Au Nanoparticles via Atomic Scale Rearrangements. *J. Phys. Chem. C* **2018**, *122*, 26214–26225. [CrossRef]
15. Shuttleworth, I. Non-linear modelling of the effects of strain on transition metal surfaces. *Chem. Phys. Lett.* **2016**, *666*, 51–57. [CrossRef]
16. Jennings, P.C.; Lysgaard, S.; Hansen, H.A.; Vegge, T. Decoupling strain and ligand effects in ternary nanoparticles for improved ORR electrocatalysis. *Phys. Chem. Chem. Phys.* **2016**, *18*, 24737–24745. [CrossRef] [PubMed]
17. Rodriguez, J. Physical and chemical properties of bimetallic surfaces. *Surf. Sci. Rep.* **1996**, *24*, 223–287. [CrossRef]
18. Yu, W.; Porosoff, M.; Chen, J.G. Review of Pt-Based Bimetallic Catalysis: From Model Surfaces to Supported Catalysts. *Chem. Rev.* **2012**, *112*, 5780–5817. [CrossRef] [PubMed]
19. Wu, J.; Yang, H. Platinum-Based Oxygen Reduction Electrocatalysts. *Acc. Chem. Res.* **2013**, *46*, 1848–1857. [CrossRef] [PubMed]
20. Shuttleworth, I. Strain engineering of H/transition metal systems. *Surf. Sci.* **2017**, *661*, 49–59. [CrossRef]
21. Kim, S.K.; Shin, K.; Henkelman, G. Stability of Pt Skin Intermetallic Core Catalysts and Adsorption Properties for the Oxygen Reduction Reaction. *J. Phys. Chem. C* **2021**, *125*, 3527–3534. [CrossRef]
22. Haile, A.S.; Yohannes, W.; Mekonnen, Y.S. Oxygen reduction reaction on Pt-skin Pt3V(111) fuel cell cathode: A density functional theory study. *RSC Adv.* **2020**, *10*, 27346–27356. [CrossRef]
23. Shuttleworth, I. The effects of strain on the ordered phases of NixPt1-x (x = 0.25, 0.5, and 0.75). *Chem. Phys. Lett.* **2017**, *689*, 41–47. [CrossRef]
24. Shuttleworth, I. Magnetism in the strained ordered phases of Pt x Fe 1-x and Pt x Co 1-x (x = 0.25, 0.5, and 0.75). *J. Phys. Chem. Solids* **2018**, *114*, 153–162. [CrossRef]
25. Stamenkovic, V.R.; Fowler, B.; Mun, B.S.; Wang, G.; Ross, P.N.; Lucas, C.A.; Marković, N.M. Improved Oxygen Reduction Activity on Pt3Ni(111) via Increased Surface Site Availability. *Science* **2007**, *315*, 493–497. [CrossRef] [PubMed]

26. Stamenkovic, V.; Mun, B.S.; Mayrhofer, K.; Ross, P.N.; Markovic, N.M.; Rossmeisl, J.; Greeley, J.; Nørskov, J.K. Changing the Activity of Electrocatalysts for Oxygen Reduction by Tuning the Surface Electronic Structure. *Angew. Chem. Int. Ed.* **2006**, *45*, 2897–2901. [CrossRef]

27. Shuttleworth, I. Controlled FCC/on-top binding of H/Pt(111) using surface stress. *Appl. Surf. Sci.* **2016**, *378*, 286–292. [CrossRef]

28. Shuttleworth, I.G. Binding Site Transitions Across Strained Oxygenated and Hydroxylated Pt(111). *ChemistryOpen* **2018**, *7*, 356–369. [CrossRef]

29. Mun, B.S.; Watanabè, M.; Rossi, M.; Stamenković, V.; Markovic, N.M.; Ross, P.N. The Study of Surface Segregation, Structure, and Valence Band Density of States of Pt3Ni(100),(110), and (111) Crystals. *Surf. Rev. Lett.* **2006**, *13*, 697–702. [CrossRef]

30. Giannozzi, P.; Andreussi, O.; Brumme, T.; Bunau, O.; Nardelli, M.B.; Calandra, M.; Car, R.; Cavazzoni, C.; Ceresoli, D.; Cococcioni, M.; et al. Advanced capabilities for materials modelling with Quantum ESPRESSO. *J. Phys. Condens. Matter* **2017**, *29*, 465901. [CrossRef]

31. Corso, A.D. Pseudopotentials periodic table: From H to Pu. *Comput. Mater. Sci.* **2014**, *95*, 337–350. [CrossRef]

32. Methfessel, M.; Paxton, A. High-precision sampling for Brillouin-zone integration in metals. *Phys. Rev. B* **1989**, *40*, 3616–3621. [CrossRef] [PubMed]

33. Vojvodic, A.; Norskov, J.K.; Abildpedersen, F. Electronic Structure Effects in Transition Metal Surface Chemistry. *Top. Catal.* **2014**, *57*, 25–32. [CrossRef]

34. Pisanty, A.; Amador-Bedolla, C.; Ruiz, Y.; de la Vega, M. Band structures of Ni3Pt and NiPt3. *Eur. Phys. J. B* **1990**, *80*, 237–239. [CrossRef]